Spin and orbital metallic magnetism in rhombohedral trilayer graphene

Chunli Huang, Tobias M. R. Wolf, Wei Qin, Nemin Wei, Igor V. Blinov, and Allan H. MacDonald

Phys. Rev. B **107**, L121405 — Published 17 March 2023

DOI: 10.1103/PhysRevB.107.L121405

Spin and Orbital Metallic Magnetism in Rhombohedral Trilayer Graphene

Chunli Huang,[1,2] Tobias M. R. Wolf,[2] Wei Qin,[2] Nemin Wei,[2] Igor V. Blinov,[2] and Allan H. MacDonald[2]

[1] *Theoretical Division, T-4, Los Alamos National Laboratory, Los Alamos, New Mexico 87545, USA*

[2] *Department of Physics, University of Texas at Austin, Austin, Texas 78712, USA*

(Dated: October 3, 2022)

We provide a theoretical interpretation of the metallic broken spin–valley (flavor) symmetry states recently discovered in hole-doped rhombohedral trilayer (ABC) graphene in large electric displacement fields. Our conclusions about the phase diagram and phase transitions combine insights from ABC graphene electronic structure models and mean field theory, and are guided by the precise magneto-oscillation Fermi-surface-area measurements of recent experiments. We find that the principle of momentum-space condensation plays a key role in determining Fermi surface reconstructions enabled by broken flavor symmetries when the single-particle bands imply thin annular Fermi seas. The reconstructed Fermi sea consists of one large outer Fermi surface enclosed majority-flavor states in reciprocal space area A_{maj} and one or more small inner hole-like Fermi surfaces enclosed minority-flavor states in A_{min} that are primarily responsible for nematic order. The competing groundstates (valley-Ising, valley-XY and spin-polarized state) have different A_{maj}/A_{min} and exchange energy maximises this ratio and selects valley-XY nematic metal as the lowest energy state. We discuss how the nematic pockets explain the observed fractionalization of quantum oscillation frequencies, and propose anisotropic transport and non-linear Hall effect as additional observables.

Introduction. Multilayer graphene systems continue to surprise researchers with unexpected states of matter. Zhou *et al.* [1–3] have recently uncovered rich phase diagrams in both bernal bilayer (AB) and rhombohedral trilayer (ABC) graphene containing half-metal, quarter-metal, partially-isospin polarized (PIP) metal, spin-triplet superconductor, and spin-singlet superconductor states in a three dimensional parameter space spanned by the electric displacement field D, the carrier density n_e, and the magnetic field B, see also Ref. [4, 5]. The origin of superconductivity has been studied in Refs. [6–13]. In this Letter, we explain the pattern of spontaneous symmetry breaking induced by Coulomb interaction and corresponding Fermi surface reconstructions observed in the metallic states of ABC trilayer graphene. We find that the magnetic order and nematic order are often intertwined at large density due to momentum space condensation [14] (c.f. valley-XY nematic metal in Fig. 1).

At low carrier densities $|n_e| \lesssim 2 \times 10^{12}$ cm^{-2} and large electric displacement fields $D \gtrsim 0.2$ V/nm, holes ($n_e < 0$) in ABC graphene occupy low velocity Bloch states [15, 16] with momenta near one of two inequivalent honeycomb lattice Brillouin-zone corners. These regions of momentum space are referred to below as valleys, and endow electrons with a valley pseudospin in addition to spin. States in the two valleys are related by time-reversal symmetry. Because the spin- ($s =\uparrow, \downarrow$) and valley- ($\tau = K, K'$) projected densities of states are identical for each spin-valley, the paramagnetic state occupies the four flavors equally. The broken spin-valley symmetry states seen experimentally occupy the four flavors unequally, just as magnetic metals occupy majority and minority spins unequally, and are expected because the Fermi energy at low carrier densities is small compared to the Coulomb energy per particle. Because of

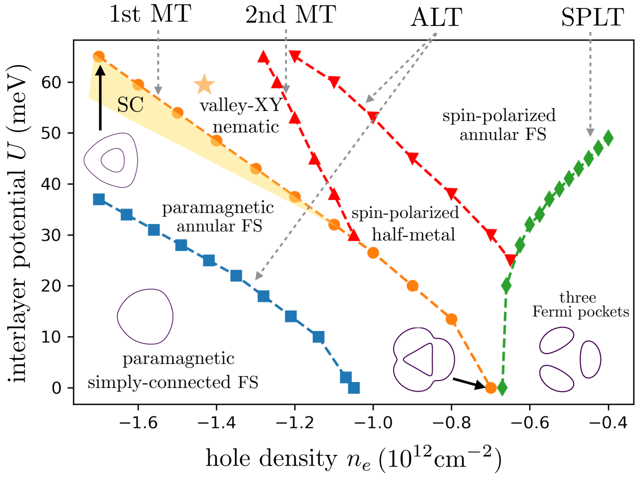

Figure 1. Zero temperature phase diagram of ABC trilayer graphene. Fermi surface topologies in the various phases are indicated schematically. The phase boundaries mark magnetic transitions (MT) and Lifshitz transitions which modify the Fermi surface topology. We distinguish two types of Lifshitz transitions, annular Lifshitz transitions (ALTs) that occur when the Fermi level crosses $\boldsymbol{k} = 0$ energy band maxima to form an electron pocket inside an annular hole Fermi sea, and saddle-point Lifshitz transitions (SPLTs) that occur when the Fermi level crosses $\boldsymbol{k} \neq 0$ energy band saddle points to break the annulus into three separate pockets. At the first magnetic transition, the paramagnetic annular Fermi sea supports a pair of Shubnikov-de Haas quantum oscillations with normalized frequencies $\boldsymbol{f}^* = (0.06, 0.31)$. The interlayer potential U is proportional to the displacement field D in the experiment. Superconductivity occurs in the region of the phase diagram shaded yellow at large hole density close to the first magnetic transition.

the high quality of the ABC graphene devices studied by Zhou *et al.*, it has been possible to measure magnetic oscillations at weak magnetic fields, and in this way to accurately measure the Fermi sea areas enclosed by most of the Fermi surfaces present in most phases. Magneto-oscillations do not on their own distinguish different symmetry-broken states and do not provide the information about Fermi surface shapes. These we infer by combining insights from ABC trilayer graphene electronic structure models and mean field theory calculations [17] that are corroborated by features that appear in resistance *vs.* n_e and D maps, in addition to the thermodynamic compressibility data [1–3]. We detail our band structure model and mean-field calculations in the Supplemental Material [17].

Fig. 1 is our main result and it explains the evolution of the ground state as the hole density decreases and interactions increase in importance. As shown in Fig. 1, at large interlayer potential U the first transition is an annular Liftshitz transition (ALT) at which an electron pocket emerges in the interior of the hole Fermi sea. This annular Fermi sea undergoes a first magnetic transition (1st MT) to a valley ordered state accompanied by a strong Fermi surface reconstruction; *i.e.*, the number of Fermi surfaces (per spin) is reduced from four to two and the annulus near $k = 0$ is removed. This state is susceptible to nematic broken symmetries that give rise to small crescent-shaped Fermi surfaces, which explain the small quantum oscillation frequencies reported in Ref. [1, 3]. We identify such a valley ordered state as a valley-XY nematic metal [18]. When the hole density is further lowered, the crescent-shaped (nematic) Fermi surface shrinks and leads to a negative electronic compressibility as reported in Figs. 1d,g of Ref. [1]. The crescent-shaped Fermi surface disappears at a second magnetic transition (2nd MT) to a spin-polarized half-metal. As the hole density is lowered even further, a second ALT changes the topology of the spin-polarized half-metal to an annular shape. Both the paramagnetic phase ALT (blue line) and the spin-polarized state ALT are prominent experimentally because they lead to easily identified peaks in resistance along the lines from $(n_e\,,\,D) = (-1.2, 0)$ to $(-1.8, 0.28)$ and from $(-0.6, 0)$ to $(-1.1, 0.5)$ in Fig. 1e of Ref. [3], respectively. At small U, there is only one magnetic transition because the paramagnetic metal avoids the transition into a valley-XY nematic metal. In what follows, we first address the instability of a paramagnetic metal with an annular Fermi sea [19], then the properties of magnetic metals.

Annular Fermi sea. Depending on n_e and U, the single-particle bands can have one of three distinct Fermi surface topologies (see Fig. 1): a simply-connected Fermi sea, a Fermi sea with three disjoint pockets, and an annular Fermi sea. With decreasing hole density, the annular topology appears at the ALT when the Fermi level intersects a shallow local valence band minimum at $\boldsymbol{k} = 0$, and persists to the saddle-point Lifshitz transition (SPLT) at which the annulus splits into three pockets and the density of states diverges logarithmically. We focus below on the experimentally demonstrated instability of the C_3-distorted annular Fermi sea, which occurs well before the SPLT is reached and is therefore not simply because of the large density of states at the Fermi level.

Each reciprocal-space area A_ν enclosed by a Fermi surface ν leads to a normalized quantum oscillation frequency

$$f_\nu = \frac{A_\nu}{(2\pi)^2\,|n_e|}, \tag{1}$$

that we interpret as fraction of (electron or hole) charge carriers in Fermi pocket ν. The annular Fermi sea has an exterior hole-like Fermi surface (with area A_{outer}) and an interior electron-like Fermi surface (with area A_{inner}), see Fig. 2(a), such that the hole carrier area is $A_0 = A_{\text{outer}} - A_{\text{inner}}$. The two Fermi surfaces lead to two quantum oscillation frequencies $\boldsymbol{f} = (f_{\text{inner}}\,,\,f_{\text{outer}})$ according to Eq. (1) [20]. The paramagnetic metal partitions holes equally into the four flavors $\alpha = \{K\uparrow, K\downarrow, K'\uparrow, K'\downarrow\}$, i.e.,

$$n_\alpha \equiv \frac{n_e}{4}\;\;\forall\,\alpha, \tag{2}$$

which implies $A_0/(2\pi)^2 = |n_e|/4$ for an annular Fermi sea.

Valley-XY nematic metal. As the inner Fermi surface of the paramagnet becomes larger, occupied hole momenta are more widely dispersed and this leads to a reduction in the long-range Coulomb exchange energy [19]. We identify this reduction as the driver of the first magnetic transition, which occurs near $A_{\text{inner}}/A_0 \approx 0.24$ and therefore with normalized quantum oscillation frequencies

$$\boldsymbol{f}^* \sim (0.06, 0.31). \tag{3}$$

The fact that these frequencies are nearly independent of U emphasizes that Fermi sea shape is more important in driving the instability than hole density.

The first magnetic transition leads to strong flavor polarization and Fermi surface reconstructions where the majority-flavor states have a large hole-like Fermi surface with no annulus. Since the outer Fermi surface A_{outer} has a large Fermi velocity, it is energetically favorable to retain a small minority-flavor hole pocket centered at $k \neq 0$ to limit its expansion. For a given n_e, the exchange energy favors the valley-XY state over the spin-polarized and valley-Ising states illustrated in Fig. 2 because the outer Fermi surface of its valley-mixed quasiparticles has C_6 symmetry and can therefore enclose a larger area for given Fermi radii. The relationship between the spin–valley SU(4) magnetic anisotropy energy and the area of the inner Fermi surface is illustrated in Fig. 2(b,c) for

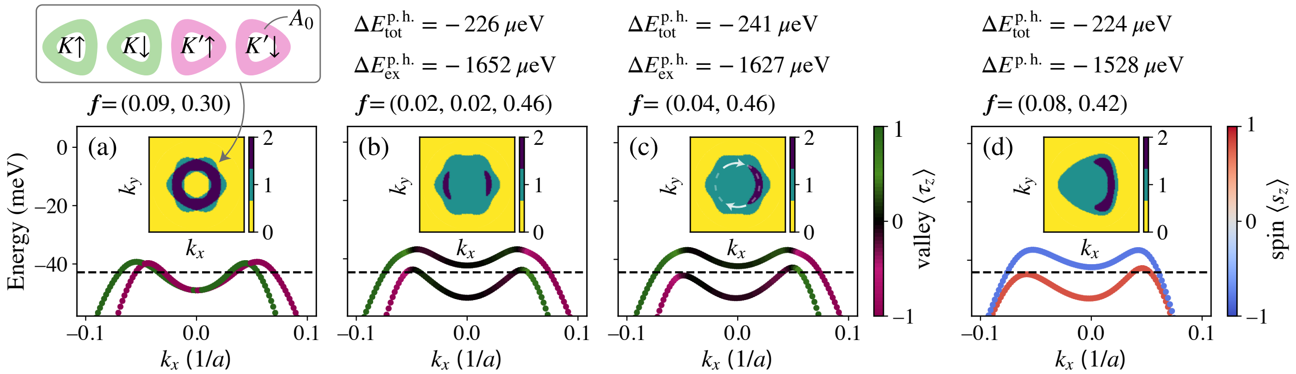

Figure 2. Mean-field valence bands and Fermi surfaces of competing states at $n_e = -1.4\times10^{12}\,\mathrm{cm}^{-2}$ and $U = 60$ meV (yellow star in Fig. 1): (a) the paramagnetic metal, (b–c) the valley-XY nematic metal and (d) the spin nematic metal. The yellow, green, and blue regions are respectively occupied by zero, one, and two holes. The paramagnetic metal has independent Fermi surfaces in all valley–spin sectors, as illustrated in panel (a). In the ordered region all magnetic states gain roughly the same amount of total energy relative to the paramagnetic state, ($\Delta E^{\rm p.h.}_{\rm tot}\sim 200\ \mu$eV for the illustrated case) by lowering exchange energy $\Delta E^{\rm p.h.}_{\rm ex}\sim 1500\ \mu$eV per hole at a cost in band energy. Their energy differences between the different ordered states (~ 1 to $20\ \mu$eV per hole) is mainly determined by the characteristics of the inner nematic Fermi sea. The magnetic anisotropic energy in the SU(4) spin–valley space first minimizes the area of the inner hole Fermi sea, measured by the quantum oscillation frequencies $\boldsymbol{f}$, and then breaks rotational symmetry to make the inner surface more compact. The arrows in (c) suggest the sliding degree-of-freedom of the crescent-shaped Fermi sea. This mean-field calculation was performed with an accuracy of $\lesssim 1\ \mu$eV per hole.

valley-XY polarized states and in Fig. 2(d) for a spin-polarized state. The first magnetic transition leads to the discontinuous changes in quantum oscillation frequencies from the paramagnetic state values $\boldsymbol{f}^*$ to the ones shown in Fig. 2. Although the candidate ordered states differ little in energy, they do have distinct quantum oscillation frequencies. The values reported in Ref. [3] support our identification of the valley-XY state as the ground state in this region of the phase diagram. Note that the quantum oscillation data put a severe constraint on the many possible magnetic states in the large SU(4) Hilbert space, see Ref. [17]. In particular, an intervalley coherent state (valley-XY) without nematicity cannot explain the sudden jump in the oscillation frequencies at the phase-boundary.

We now explain the crescent shape of the reconstructed inner Fermi sea of the valley-XY metal shown in Fig. 2(c). Note first that the valence bands have a ring of maxima at $\boldsymbol{k}_{\rm VBM}\sim k_0(\cos(\theta),\sin(\theta))$ where $k_0a\sim 0.05$ and $2\pi > \theta \geq 0$. When a point on the ring rises above the Fermi level it nucleates a hole-like Fermi sea. Such Fermi sea nucleation can be understood as a form of momentum-space condensation introduced by Heisenberg [14]. Because the energy dispersion along the radial direction is steep, due mainly to strong non-local exchange-splitting, whereas the dispersion along the ring of valence band maximum is anomalously flat, the nucleated Fermi sea has the shape of a crescent. Furthermore, the crescent Fermi sea wants to be as compact as possible to increase the exchange energy from the long-range Coulomb interaction. Thus, although the reconstructed inner Fermi seas in Fig. 2(b,c) have the same area, their total energy differ because of the relative compactness of their Fermi seas. The single-crescent state is the most compact and hence has the lowest energy.

The order parameter of the crescent Fermi sea can be characterized by a traceless symmetric tensor

$$\hat{N}_{ij} = \hat{\mathcal{D}}_{ij} - \frac{1}{2}\,\mathrm{tr}\left(\hat{\mathcal{D}}\right)\delta_{ij}, \tag{4}$$

where $i,j\in\{x,y\}$ and $\hat{\mathcal{D}}$ is the Drude tensor

$$\hat{\mathcal{D}}_{ij} = \sum_{\nu=1,2\ldots N_F}\int\left(\frac{v_{\nu,i}v_{\nu,j}}{|\boldsymbol{v}_\nu|}\right)\frac{dk_{\parallel,\nu}}{(2\pi)^2\hbar}. \tag{5}$$

Here $\boldsymbol{v}_\nu(\boldsymbol{k}) = \nabla\epsilon_\nu(\boldsymbol{k})$ is the Fermi velocity and $\nu = 1,2,\ldots,N_F$ enumerates the Fermi surfaces. The eigenvalues of $\hat{N}_{ij}$ define a nematic order parameter $\mathcal{N} = |\det\hat{\mathcal{D}}|^{1/2}/\,\mathrm{tr}\,\hat{\mathcal{D}}$. The values for the single-crescent and double-crescent states are $\mathcal{N} = 4\%$ and $\mathcal{N} = 6\%$, respectively. This nematicity can lead to transport anisotropy below the transition temperature, that we predict will be most prominent close to the phase boundary of the first magnetic transition. While the single-crescent nematic Fermi sea breaks time-reversal symmetry, the resulting intrinsic anomalous Hall conductivity is negligible $\sigma_{xy}\sim 10^{-7}e^2/h$. This is because the Bloch-bands in the valley-XY state are topologically-trivial (with zero Chern number) and the Berry-curvature changes rapidly along the single-crescent Fermi surface. Nevertheless, the nematic state leads to a significant Berry-curvature dipole

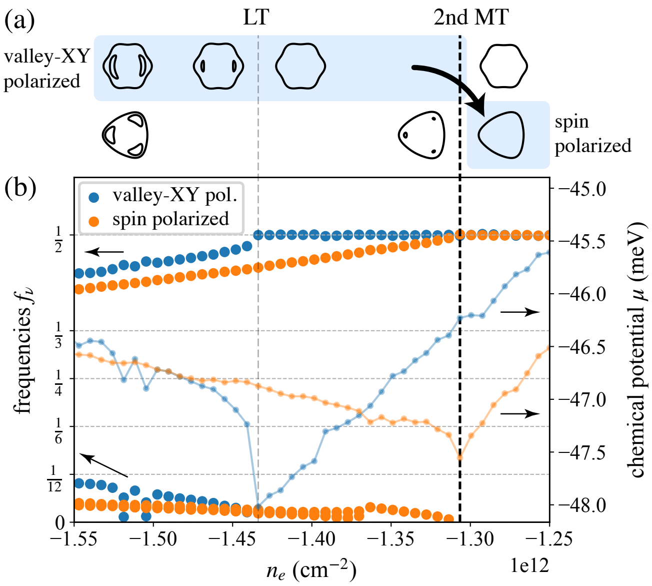

Figure 3. Transition from a nematic valley-XY phase to the valley-XY half-metal and to the spin-polarized half-metal as a function of decreasing hole density n_e at fixed interlayer potential $U = 62$ meV. (a) The evolution of the Fermi sea for valley-XY and spin ordered states, where the ground states are shaded light blue. The valley-XY ordered state undergoes a Lifshitz transition (LT) upon which it loses its inner pockets before going through the second magnetic transition (2nd MT). (b) Quantum oscillation frequencies f_ν (big markers) of the Fermi surfaces shown in panel (a), and chemical potential μ (small markers) as the electron density increases.

[21]

$$\boldsymbol{\Lambda} = \sum_{\nu=1,2\ldots N_F} \int \left(\Omega_\nu \frac{\boldsymbol{v}_\nu}{|\boldsymbol{v}_\nu|} \right) \frac{dk_{\parallel,\nu}}{(2\pi)^2\hbar}, \tag{6}$$

where Ω_ν is the Berry curvature evaluated on the Fermi surface ν. For the single-crescent state in Fig. 2(c), we find $|\boldsymbol{\Lambda}| \simeq 0.26\,a \sim 0.7A^\circ$ [17] which is comparable to the Berry curvature dipole estimated experimentally in other systems [22] so this is potentially observable through the non-linear Hall measurement [21, 23].

The crescent Fermi sea is fragile in the sense that it costs very little energy to deform and slide it around the ring of valence band maxima at $\boldsymbol{k}_{\rm VBM}$ as indicated in Fig. 2(c). We can control the center of the crescent Fermi sea on $\boldsymbol{k}_{\rm VBM}$ by minimising $\tilde{H} = H^{\rm MF} - \mu_{\rm nem}\,\rho(\boldsymbol{k}_{\rm VBM})$ where $\mu_{\rm nem}$ is a Lagrange multiplier, $H^{\rm MF}$ is the mean-field Hamiltonian, and $\rho(\boldsymbol{k}_{\rm VBM})$ is the density matrix at $\boldsymbol{k}_{\rm VBM}$ [17]. The pinning potential which favors particular crescent orientations is $\lesssim 1$ μeV per hole [24]. When the crescent Fermi sea becomes small, it costs very little energy to split it into two or more smaller crescents. We attribute the fractionalization of the small quantum oscillation frequencies reported in Ref. [3] as the system advances deeper into the valley-XY phase, to this fragility.

Second magnetic transition. As the hole density decreases in the valley-XY metal phase, the paramagnetic region enclosed by the crescent Fermi sea shrinks as shown in Fig. 3(a) and increases the valley-XY order parameter. This leads to a decrease of chemical potential μ as shown in Fig. 3(b) and explains the observed (slightly) negative inverse compressibility $\kappa = \partial\mu/\partial n_e$ in the PIP phase of Ref. [1]. Note that the sharp drop in chemical potential close to $n_e \sim -1.51 \times 10^{12}$ cm^{-2} and -1.52×10^{12} cm^{-2} is because the exchange energy becomes more negative when one of the two nematic pockets shown in Fig. 3(a) becomes significantly larger than the other. This leads to a bifurcation of the small frequency. When the nematic Fermi sea disappears completely, $\mathcal{N} = 0$ and $\boldsymbol{f} = (0, 0.5)$. The valley-XY half-metal is then characterized by a single compact Fermi surface with C_6 rotational symmetry (for each spin). Although the C_6 Fermi surface is closer to a circle, compared to the spin-polarized half-metal which only has C_3, the content of the wavefunction in the valley-XY metal changes dramatically over the enclosed area. The valley-XY half-metal eventually undergoes a second magnetic transition to a spin-polarized half-metal, as shown in Fig. 1 and indicated by the arrow in Fig. 3(a). Although this is a first-order phase transition, there is no change in $\boldsymbol{f}$ because both states are half-metals, and no change in $\mathcal{N}$ because both states lack nematicity. Their phase boundary, however, can easily be shifted by an in-plane spin-polarizing Zeeman field [1–3]. The transition to the spin-polarized half-metal can be understood as a reset transition [1, 25–27], at which the minority spin Hilbert space becomes inactive while there is still equipartition of density in the majority spin Hilbert space:

$$n_{K\uparrow} = n_{K'\uparrow} = \frac{n_e}{2} \quad , \quad n_{K\downarrow} = n_{K'\downarrow} = 0. \tag{7}$$

As the hole density is lowered, a Lifshitz transition creates an annular topology in the (majority) ↑-spin Fermi sea and the same symmetry-breaking pattern repeats in the ↑-spin Hilbert space as the density of holes is further lowered.

Spin-fluctuation and spin-orbit interactions. At weaker displacement fields, the Fermi velocity of the outer Fermi surface is smaller at the first magnetic transition than it is at large $U, |n_e|$, especially where it is close to the three SPLT momenta. It is hence favorable to make a direct transition from the paramagnetic state to the spin-polarized half-metal [28]. Proximity to a transition between a paramagnetic metal and a ferromagnetic metal is known to suppress spin singlet superconductivity [29] and valley-singlet superconductivity [30], explaining the termination of singlet superconductivity at small D seen in Ref. [3], which occurs despite an increasing density of states. The direct transition from the paramagnetic state to the spin-polarized half-metal leads to a sudden jump of quantum oscillation frequencies directly from $\boldsymbol{f}^*$ to $\boldsymbol{f} = (0, 0.5)$. In our mean-field calculations, this direct transition continues to zero displacement field ($U = 0$), as shown in Fig. 1. In experiment, however, the magnetic phase fades away at small displacement field and blends into the paramagnetic phase. We attribute this behavior to spin fluctuations that become important when the electric displacement field is small. The displacement field can suppress spin fluctuations because it increases the strength of spin-orbit coupling [31–33], providing the magnetic anisotropy needed for spin-order.

Summary and discussion. The magnetic order recently discovered [1–3] in metallic ABC trilayer graphene is unusual because it involves valley as well as spin degrees of freedom, and because the quasiparticle bands imply that the unordered paramagnetic states have annular Fermi seas. By combining mean-field theory with a model that captures pertinent electronic structure details, we are able to account for the phase transitions observed experimentally and shed light on the nature of the different phases. In particular we identify the experimental partially-isospin-polarized (PIP) state as a valley-XY nematic metal. A potential direct probe for such order is the atomic-scale local density of states, as was recently observed in scanning-tunneling microscopy measurements of a valley-XY magnetic insulator under strong magnetic field [34]. We find that, as in conventional itinerant electron magnets, the magnetic condensation energy greatly exceeds a much smaller magnetic anisotropy energy. The SU(4) spin–valley magnetic anisotropy energy controls a competition between valley and spin-polarized states, which are very close in energy throughout the phase diagram. We predict that the valley-XY metal, which is stabilized at large interlayer potential, is nematic because small minority-hole pockets break rotational symmetries in order to become more compact, driven by the energetic expense of expanding the outer Fermi surface. The nematicity of these states should be observable through transport anisotropy and the non-linear Hall effect. When the minority-holes are absent at low hole densities and at low displacement fields, spin order is preferred over valley order. In closing, let us briefly mention the possibility for the small nematic Fermi sea to crystallize into a Wigner crystal state that breaks both translation and C_3 symmetry. In the spirit of Ref. [35], at sufficiently low density of holes, such anisotropic Wigner crystal states can have lower energy than the nematic fluid and conventional hexagonal Wigner crystal states due to the ring of Van Hove singularities in k-space.

Note added. Recently, we found that Ref. [36] discusses momentum condensation (“flocking” effect) in Bernal bilayer graphene with three disjoint Fermi pockets whose microscopic origin is similar to the formation of nematic Fermi surface we discuss here in ABC trilayer graphene.

Acknowledgments. We thank Anna Seiler, Andrea Young and Haoxin Zhou for informative discussions. The work done at LANL was carried out under the auspices of the US DOE NNSA under Contract No. 89233218CNA000001 through the LDRD Program. This work done at UT Austin is supported by the U.S. Department of Energy, Office of Science, Basic Energy Sciences, under Award DE-SC0022106. T.M.R.W. is grateful for the financial support from the Swiss National Science Foundation (Postdoc.Mobility Grant No. 203152).

[1] H. Zhou, T. Xie, A. Ghazaryan, T. Holder, J. R. Ehrets, E. M. Spanton, T. Taniguchi, K. Watanabe, E. Berg, M. Serbyn, and A. F. Young, Half and quarter metals in rhombohedral trilayer graphene, Nature **598**, 429 (2021), arXiv:2104.00653.

[2] H. Zhou, Y. Saito, L. Cohen, W. Huynh, C. L. Patterson, F. Yang, T. Taniguchi, K. Watanabe, and A. F. Young, Isospin magnetism and spin-triplet superconductivity in Bernal bilayer graphene, (2021), arXiv:2110.11317 [cond-mat].

[3] H. Zhou, T. Xie, T. Taniguchi, K. Watanabe, and A. F. Young, Superconductivity in rhombohedral trilayer graphene, Nature **598**, 434 (2021), arXiv:2106.07640.

[4] A. M. Seiler, F. R. Geisenhof, F. Winterer, K. Watanabe, T. Taniguchi, T. Xu, F. Zhang, and R. T. Weitz, Quantum cascade of new correlated phases in trigonally warped bilayer graphene, arXiv preprint arXiv:2111.06413 (2021).

[5] S. C. de la Barrera, S. Aronson, Z. Zheng, K. Watanabe, T. Taniguchi, Q. Ma, P. Jarillo-Herrero, and R. Ashoori, Cascade of isospin phase transitions in Bernal bilayer graphene at zero magnetic field, arXiv e-prints , arXiv:2110.13907 (2021), arXiv:2110.13907 [cond-mat.mes-hall].

[6] S. Chatterjee, T. Wang, E. Berg, and M. P. Zaletel, Intervalley coherent order and isospin fluctuation mediated superconductivity in rhombohedral trilayer graphene, (2021), arXiv:2109.00002 [cond-mat].

[7] A. Ghazaryan, T. Holder, M. Serbyn, and E. Berg, Unconventional superconductivity in systems with annular fermi surfaces: Application to rhombohedral trilayer graphene, Physical review letters **127**, 247001 (2021).

[8] Y.-Z. You and A. Vishwanath, Kohn-Luttinger Superconductivity and Inter-Valley Coherence in Rhombohedral Trilayer Graphene, arXiv e-prints , arXiv:2109.04669 (2021), arXiv:2109.04669 [cond-mat.str-el].

[9] T. Cea, P. A. Pantaleón, V. T. Phong, and F. Guinea, Superconductivity from repulsive interactions in rhombohedral trilayer graphene: A Kohn-Luttinger-like mechanism, Phys. Rev. B **105**, 075432 (2022), arXiv:2109.04345 [cond-mat.mes-hall].

[10] W. Qin, C. Huang, T. M. R. Wolf, N. Wei, I. V. Blinov, and A. H. MacDonald, Functional Renormalization Group Study of Superconductivity in Rhombohedral Trilayer Graphene, arXiv e-prints , arXiv:2203.09083 (2022), arXiv:2203.09083 [cond-mat.supr-con].

[11] A. L. Szabó and B. Roy, Metals, fractional metals, and superconductivity in rhombohedral trilayer graphene, Physical Review B **105**, L081407 (2022).

[12] Z. Dong and L. Levitov, Superconductivity in the vicinity of an isospin-polarized state in a cubic dirac band, arXiv preprint arXiv:2109.01133 (2021).

[13] Y.-Z. Chou, F. Wu, J. D. Sau, and S. D. Sarma, Acoustic-phonon-mediated superconductivity in rhombohedral trilayer graphene, Physical review letters **127**, 187001 (2021).

[14] W. Heisenberg, Two lectures, in *Scientific Review Papers, Talks, and Books Wissenschaftliche Übersichtsartikel, Vorträge und Bücher*, edited by W. Blum, H.-P. Dürr, and H. Rechenberg (Springer Berlin Heidelberg, Berlin, Heidelberg, 1984) pp. 443–455.

[15] F. Zhang, B. Sahu, H. Min, and A. H. MacDonald, Band structure of A B C -stacked graphene trilayers, Phys. Rev. B **82**, 035409 (2010).

[16] E. McCann and M. Koshino, The electronic properties of bilayer graphene, Rep. Prog. Phys. **76**, 056503 (2013), arXiv:1205.6953.

[17] See Supplemental Material for details on the band structure model, the Coulomb interaction potential, the self-consistent Hartree-Fock approximation, and a discussion of intervalley coherent states without nematicity.

[18] Note that other works sometimes refer to valley-XY ordered states as 'intervalley coherent states'.

[19] J. Jung, M. Polini, and A. H. MacDonald, Persistent current states in bilayer graphene, Physical Review B **91**, 155423 (2015).

[20] We group the frequencies into a vector for convenience. Note that the number of entries is equal to the number Fermi pockets, and that we order the frequencies from lowest to highest.

[21] I. Sodemann and L. Fu, Quantum nonlinear hall effect induced by berry curvature dipole in time-reversal invariant materials, Phys. Rev. Lett. **115**, 216806 (2015).

[22] Q. Ma, S.-Y. Xu, H. Shen, D. MacNeill, V. Fatemi, T.-R. Chang, A. M. Mier Valdivia, S. Wu, Z. Du, C.-H. Hsu, *et al.*, Observation of the nonlinear hall effect under time-reversal-symmetric conditions, Nature **565**, 337 (2019).

[23] S. Sinha, P. C. Adak, A. Chakraborty, K. Das, K. Debnath, L. D. V. Sangani, K. Watanabe, T. Taniguchi, U. V. Waghmare, A. Agarwal, and M. M. Deshmukh, Berry curvature dipole senses topological transition in a moiré superlattice, Nature Physics **18**, 765 (2022).

[24] We used a triangular k-grid with 140×140 point-resolution in regions up to radii $k_{\max}a = 0.2$.

[25] U. Zondiner, A. Rozen, D. Rodan-Legrain, Y. Cao, R. Queiroz, T. Taniguchi, K. Watanabe, Y. Oreg, F. von Oppen, A. Stern, *et al.*, Cascade of phase transitions and dirac revivals in magic-angle graphene, Nature **582**, 203 (2020).

[26] Y. Saito, F. Yang, J. Ge, X. Liu, T. Taniguchi, K. Watanabe, J. Li, E. Berg, and A. F. Young, Isospin pomeranchuk effect in twisted bilayer graphene, Nature **592**, 220 (2021).

[27] D. Wong, K. P. Nuckolls, M. Oh, B. Lian, Y. Xie, S. Jeon, K. Watanabe, T. Taniguchi, B. A. Bernevig, and A. Yazdani, Cascade of electronic transitions in magic-angle twisted bilayer graphene, Nature **582**, 198 (2020).

[28] The groundstate energy of a spin-polarized half-metal and a valley-polarized half-metal appear to be almost degenerate due to the $SU(4)$ invariant Coulomb interaction.

[29] N. Berk and J. Schrieffer, Effect of ferromagnetic spin correlations on superconductivity, Physical Review Letters **17**, 433 (1966).

[30] C. Huang, N. Wei, W. Qin, and A. MacDonald, Pseudospin paramagnons and the superconducting dome in magic angle twisted bilayer graphene, arXiv preprint arXiv:2110.13351 (2021).

[31] S. Konschuh, M. Gmitra, D. Kochan, and J. Fabian, Theory of spin-orbit coupling in bilayer graphene, Physical Review B **85**, 115423 (2012).

[32] D. Huertas-Hernando, F. Guinea, and A. Brataas, Spin-orbit coupling in curved graphene, fullerenes, nanotubes, and nanotube caps, Physical Review B **74**, 155426 (2006).

[33] H. Min, J. Hill, N. A. Sinitsyn, B. Sahu, L. Kleinman, and A. H. MacDonald, Intrinsic and rashba spin-orbit interactions in graphene sheets, Physical Review B **74**, 165310 (2006).

[34] X. Liu, G. Farahi, C.-L. Chiu, Z. Papic, K. Watanabe, T. Taniguchi, M. P. Zaletel, and A. Yazdani, Visualizing broken symmetry and topological defects in a quantum hall ferromagnet, Science **375**, 321 (2022).

[35] E. Berg, M. S. Rudner, and S. A. Kivelson, Electronic liquid crystalline phases in a spin-orbit coupled two-dimensional electron gas, Phys. Rev. B **85**, 035116 (2012).

[36] Z. Dong, M. Davydova, O. Ogunnaike, and L. Levitov, Isospin ferromagnetism and momentum polarization in bilayer graphene, arXiv e-prints , arXiv:2110.15254 (2021), arXiv:2110.15254 [cond-mat.mes-hall].